HHS Public Access

Author manuscript

Cancer Res. Author manuscript; available in PMC 2021 July 01.

Transcriptional repression of SIRT3 potentiates mitochondrial aconitase activation to drive aggressive prostate cancer to the bone

Abhisha Sawant Dessai[1,#], **Mayrel Palestino Dominguez**[1,#], **Uan-I Chen**[2], **John Hasper**[1], **Christian Prechtl**[1], **Cuijuan Yu**[2], **Eriko Katsuta**[3], **Tao Dai**[1], **Bokai Zhu**[4], **Sung Yun Jung**[2,5], **Nagireddy Putluri**[2], **Kazuaki Takabe**[3], **Xiang H. Zhang**[2], **Bert W. O'Malley**[2], **Subhamoy Dasgupta**[1]

[1]Department of Cell Stress Biology, Roswell Park Comprehensive Cancer Center, Buffalo, NY 14263.

[2]Department of Molecular and Cellular Biology, Baylor College of Medicine, Houston, TX 77030.

[3]Department of Surgical Oncology, Roswell Park Comprehensive Cancer Center, Buffalo, NY 14263

[4]Department of Medicine, University of Pittsburgh School of Medicine, Pittsburgh, PA 15219.

[5]Department of Biochemistry, Baylor College of Medicine, Houston, TX 77030.

Abstract

Metabolic dysregulation is a known hallmark of cancer progression, yet the oncogenic signals that promote metabolic adaptations to drive metastatic cancer remain unclear. Here we show that transcriptional repression of mitochondrial deacetylase sirtuin 3 (SIRT3) by androgen receptor (AR) and its coregulator steroid receptor coactivator (SRC-2) enhances mitochondrial aconitase (ACO2) activity to favor aggressive prostate cancer. ACO2 promoted mitochondrial citrate synthesis to facilitate *de novo* lipogenesis, and genetic ablation of ACO2 reduced total lipid content and severely repressed *in vivo* prostate cancer progression. A single acetylation mark lysine258 on ACO2 functioned as a regulatory motif, and the acetylation-deficient Lys258Arg-mutant was enzymatically inactive and failed to rescue growth of ACO2-deficient cells. Acetylation of ACO2 was reversibly regulated by SIRT3, which was predominantly repressed in many tumors including prostate cancer. Mechanistically, SRC-2 bound AR formed a repressive

complex by recruiting histone deacetylase 2 (HDAC2) to the SIRT3 promoter, and depletion of SRC-2 enhanced SIRT3 expression and simultaneously reduced acetylated-ACO2. In human prostate tumors, ACO2 activity was significantly elevated and increased expression of SRC-2 with concomitant reduction of SIRT3 was found to be a genetic hallmark enriched in prostate cancer metastatic lesions. In a mouse model of spontaneous bone metastasis, suppression of SRC-2 reactivated SIRT3 expression and was sufficient to abolish prostate cancer colonization in the bone microenvironment, implying this nuclear-mitochondrial regulatory axis is a determining factor for metastatic competence.

Graphical Abstract

Nuclear-mitochondrial signaling driving prostate cancer metastasis to the bone.
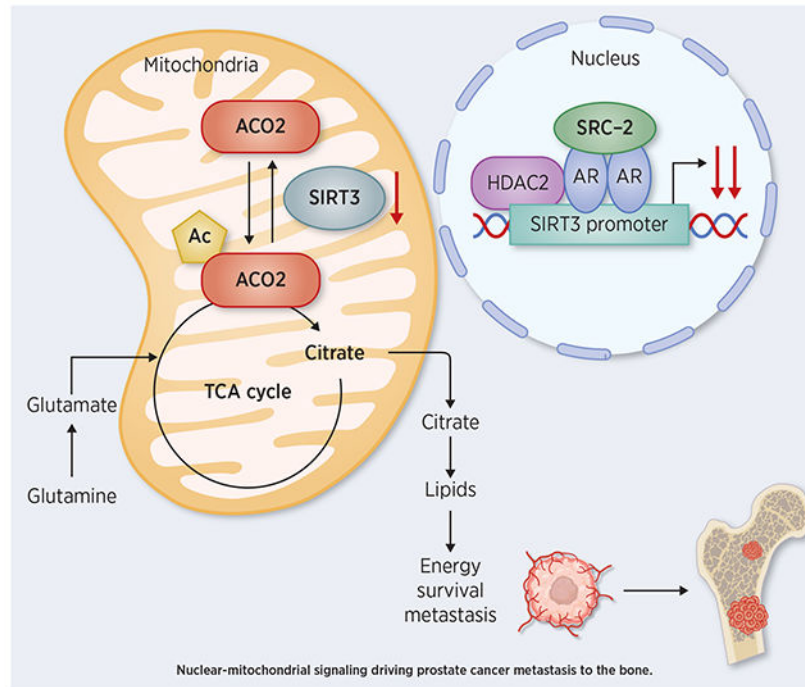
Introduction

Metabolic adaptation is one of the essential hallmarks of cancer to sustain replication and survival stress (1). Based on available nutrients, tumor cells alter their metabolic pathways for the biosynthesis of macromolecules and mitochondrial ATP synthesis. Metabolic reprogramming plays a pivotal role in tumor cell survival during metastatic dissemination, circulation, and colonization in distant organs, thus driving the successful formation of metastatic lesions (2). Hence, understanding the metabolic checkpoints that drive aggressive metastatic cancer holds promise as an effective therapeutic strategy.

Dysregulation of lipid metabolism is a hallmark of prostate cancer progression (3). In prostate tumors, there is an increased demand for *de novo* lipogenesis, which is supported by elevated levels of rate limiting enzymes such as fatty acid synthase (FASN) and stearoyl-CoA Desaturase (SCD) (4). Expression of these genes are regulated by transcription factors sterol regulatory element-binding protein 1 (SREBP1) and androgen receptor (AR) (5), and

coregulated by steroid receptor coactivator-2 (SRC-2; also known as NCOA2/GRIP1/TIF2). SRC-2 is highly amplified and overexpressed in advanced prostate cancer patients (6) causing stimulation of lipogenesis by elevating the expression of FASN and SCD even in castrate amounts of circulating androgen (7). Despite this knowledge, it remains largely unknown how these nuclear transcriptional regulators communicate with mitochondrial machineries to drive a sustained flow of carbon flux to support elevated demands for lipids.

Mitochondrial citrate is the precursor metabolite required for lipogenesis, which is exported to the cytosol for conversion into acetyl-CoA and subsequently into malonyl CoA for *de novo* biosynthesis of fatty acids (8). The regulation of citrate metabolism is unique in prostate glands compared to other organs. Normal prostatic cells mostly depend on diet-derived lipids for fatty acid synthesis and secrete a large amount of citrate into the prostatic fluid as an energy source for sperm (9). This is biochemically achieved by increasing the influx of zinc into the mitochondria, which functions as a competitive inhibitor of aconitase 2 (ACO2) enzyme, a reversible enzyme that catalyzes the stereo-specific isomerization of citrate to isocitrate via cis-aconitate (10). Regulation of ACO2 enzyme activity is pivotal to maintain increased levels of citrate in prostate tumors, and mutations in TCA enzymes such as IDH1 frequently observed in other cancer types are rare in prostate adenocarcinoma. During prostate cancer progression, zinc import into the mitochondria is reduced and in absence of the competitive inhibitor, ACO2 enzyme becomes functional (11). The increased demand for citrate is facilitated by ACO2, however the underlying mechanisms and regulatory signals that directly potentiate the sustained activity of the enzyme remains elusive. Since reactivation of ACO2 is a biochemical feature during prostate cancer progression (12), we asked the question of whether this enzymatic regulation functions as the essential metabolic adaptive response to drive lethal prostate cancer. Moreover, none of the studies have yet investigated the mechanisms that escalate the sustained ACO2 enzymatic activity, nor do we know whether this metabolic regulation is vital for progression of the disease to distant organs. In the present study, we sought to identify the molecular functions of ACO2 in prostate cancer and define the mechanisms regulating its sustained enzyme activity, with the anticipation that these mitochondrial programming could serve as fundamental determinants of metastatic competence.

Materials and Methods

Cell Lines and in vitro culture

Prostate cancer cell lines LNCaP, 22Rv1, PC-3, and C4-2 (a gift from Dr. Weigel, Baylor) cell lines were cultured in RPMI 1640 (Gibco) supplemented with 10% FBS (Gibco) and 1% antibiotic-antimycotic (Gibco). Prostate cancer cell lines VCaP and DU145 and Human embryonic kidney cell line HEK293T were cultured in DMEM (Gibco) supplemented with 10% FBS and 1% antibiotic-antimycotic. TRAMP-C2 cell line was cultured in DMEM supplemented with 5% FBS, 5% Nu-Serum IV, 0.005 mg/ml bovine insulin and 10 nm DHT. Normal prostate cell line RWPE-1 was maintained in Keratinocyte-SFM (Gibco) medium supplemented with 1% antibiotic-antimycotic. All cell lines were obtained from ATCC and cultured at 37°C with 5% CO_2. For nutrient stressed experiment, RPMI with no glutamine (21870, Invitrogen) was used and supplemented with 10% dialyzed FBS (Gibco), and 1%

antibiotic-antimycotic (Gibco). All lines were routinely tested for mycoplasma using MycoAlter mycoplasma detection (Lonza, LT07-318), STR profile tested, and cultured for 10 passages after thawing.

Vectors and virus production

Vectors expressing shRNA targeting ACO2 (Mature Antisense: AGATTGGCAATGTCTTCCC; Clone ID: V3LHS_340894, Open Biosystems) were obtained from CBASS-core facility at Baylor. Cells were transduced with pGIPZ-shNT (non-targeting) and pGIPZ-shACO2, in presence of polybrene (Sigma, TR-1003-G) to increase the efficacy of transduction. Cells were trypsinized four days after infection and used for viability, proliferation assay and immunoblotting experiments. C4-2 and 22Rv1 cells with SRC-2 knockdown C4-2-sh18 (stable expression of shSRC-2 clone#186064), and C4-2-sh19, 22Rv1-sh19 (stable expression of shSRC-2 clone#199063) and C4-2-NT, 22Rv1-shNT (stable expression of non-targeting shRNA) were generated as described before (7). Cells were seeded at a very low density in a $10cm^2$ plate and a pooled populations of stable cell lines with SRC-2 knockdown were selected by treating cells with 1.5ug/uL puromycin. HEK293T cells were transfected with 25 μg of SIRT3-WT (Addgene #13814) and catalytic-dead mutant SIRT3 (Addgene #24492) plasmid for 4 days. TRAMP-C2 cells were transduced with adenovirus Adv-GFP or Adv-SIRT3 (Vector Biolabs # 1499) and incubated for 4 days before cellular fractionation studies.

Generation of ACO2-CRISPR-Cas9 cells

Three different clones of all-in-one lenti-U6-ACO2 gRNA-Cas9-puro vectors were obtained from Baylor CBASS core. C4-2 and 22Rv1 cells were transduced with the packaged lentiviruses. Four days after transduction, cells were trypsinized and seeded at a very low density into 15-cm dishes. Cells were selected under 1 μg/mL puromycin.

siRNA-mediated knockdown of AR

Pool of siRNA targeting AR (Dharmacon) was used to knockdown AR, and non-targeting siRNA pool was used as a control. C4-2 and LNCaP Cells were seeded in 6 well plates. After 24hrs, at 50% confluency, cells were transfected with 25 nM siRNA along with Lipofectamine 2000 (Invitrogen) and incubated for 4 days.

Generation of K258R mutated ACO2

ACO2 K258R mutant clones were generated using QuickChange Lightning Multi Site-Directed Mutagenesis Kit (Agilent, 210515) according to the manufacturer's instructions and sequence was verified. Plasmid template used for mutagenesis is Lenti ORF clone of Human aconitase 2, Myc-DDK-tagged (Origene, RC204307L1). ACO2 K258R mutation was added into the template DNA using following mutagenic primer (a773g F'): gcaggcatcctcacggtgagaggtggcaca.

RNA isolation and RTPCR

RNA was isolated using RNeasy Mini kit (QIAGEN, 74106). cDNA was synthesized by SuperScript VILO cDNA synthesis kit (Invitrogen, 11754050). qPCR was conducted with

SYBR™ Green PCR Master Mix (Invitrogen, 4309155), using Applied Biosystems™ QuantStudio™ 6 Flex Real-Time PCR System and results were analyzed by Applied Biosystems software.

Immunoblotting

Cells were lysed in NP40 (Thermo, FNN0021) supplemented with protease and phosphatase inhibitor for 30 min on ice. Protein concentration was estimated using micro BCA protein assay kit (Thermo, 23235). A detailed protocol for immunoblotting is provided in the supplementary methods.

Viability assay

Cells were seeded in 96-well plates at a density of 2×10^3 cells/well (C4-2-shNT, C4-2-shACO2, n=10) or 3×10^4 cells/well (C4-2-WT, C4-2 ACO2-KD, n=8). Cell viability was measured using CellTiter-Glo® Luminescent Cell Viability Assay kit (Promega, G7572) until day 6, according to the manufacturer's instructions. Data were analyzed by normalizing the values of each day to those of day one. The difference in viability was then compared by the fold change.

Proliferation assay

Cells were seeded into a 6-well plate at a density of 5×10^4 cells/well (C4-2 shNT, C4-2 shACO2) or 7.5×10^4 cells/well (C4-2-WT, C4-2 ACO2-KD) or 2.5×10^4 cells/well (22Rv1, 22Rv1-ACO2-KO1 and 22Rv1-ACO2-KO2). Difference in cell proliferation was measured by counting cell number in triplicate for each time point of each group. Lentivirus expressing Myc-ACO2-WT (Origene, RC204307) and myc-ACO2-K258R mutant were transduced in C4-2-ACO2-KD to rescue ACO2 expression. About 48hrs after transduction, cells were trypsinized and seeded in 6-well plates at a density of 50,000 cells/well in triplicate for day 1, 5 and 7. Cell numbers were counted (Cell Counter, Life Technologies) in triplicate for each well at above mentioned time points. Immunoblot analysis was performed on day 7 to confirm the rescue of ACO2 expression in C4-2-ACO2-KD cells. C4-2 cells were transduced with Adv-SIRT3 (Signagen, 1499) or control Adv-GFP. After 3 days of transduction, 10,000 cells/well were seeded with 12 replicates for each day in 96 well-plates. Cell proliferation was measured on days 2, 4 and 6 using CellTiter 96 Aqueous One solution cell proliferation assay kit (Promega, G3581).

Extracellular Flux assay

C4-2-WT and C4-2-ACO2-KD cells were seeded in XF microplate (Agilent, 100777-004) at a density of 2.5×10^4 cells/well and cultured overnight in complete RPMI culture media. On the day of the experiment, media was changed to Seahorse XF base medium (Agilent, 103334) supplemented with 11mM glucose, 2mM glutamine, and 1mM sodium pyruvate. Oxygen consumption rates were measured sequentially before and after the addition of oligomycin (2μM), FCCP (1μM), and antimycin A (1μM) by XF24 Extracellular Flux Analyzer according to manufacturer's instructions.

Oil O red staining of C4-2-WT and C4-2-ACO2-KO cells:

C4-2-WT and C4-2-ACO2-KD cells were seeded in a 35-mm glass bottom culture dish (Mattek, P35G-1.5-14-C), and after reaching 80% confluency, cells were stimulated with or without glutamine (2mM) for 72 hours. Cells were then fixed and stained with Oil O Red (Cayman Chemical, 600045) followed by microscopy (100x oil immersion) (7).

Isotope labeling and profiling by targeted MS

Metabolic tracing experiments were performed as described before (7, 13). C4-2-WT, C4-2-ACO2-KD1, and C4-2-ACO2-KD2 cells were seeded in 10 cm^2 plates in complete RPMI media. At 75% confluency, cells were glutamine starved for 3hrs and stimulated with 2.0 mM [U-^{13}C$_5$] glutamine (Cambridge Isotope Laboratories, Cat#CLM-1822-H) supplemented in RPMI [−] glutamine with 10% dialyzed FBS and 1% antibiotic-antimycotic. A detailed method is described in the supplementary section.

Steady state metabolomics

Steady-state metabolomics was performed to study the changes in lipid profile and TCA cycle flux with the knockdown of ACO2 in PCa cell lines C4-2 and 22Rv1. Approximately, 8X10^6 cells of C4-2-WT, C4-ACO2-KD1, C4-2-ACO2-KD2 cells, and 10X10^6 cells of 22Rv1-WT, 22Rv1-ACO2-KO1, and 22Rv1-ACO2-KO2 cells were seeded in a 10cm^2 plate for 48hrs. Media was aspirated off and the plates were washed with PBS. The plates were snap-frozen in liquid nitrogen and stored at −80°C. A detailed description for sample preparation and metabolite measurement is in the supplementary section.

Immunofluorescent staining

PC-3 cells were seeded onto coverslips. Cells were transfected either with 5 μg WT or K258R mutated ACO2 plasmids (Origene, RC204307) for 48 hours. Cells were stained with mitotracker (Invitrogen, M7512), followed by fixation in ice-cold 100% MeOH at 4°C for 10 min and then 4% PFA/PBS at RT for 30 min. After fixation, cells were permeabilized in 0.25% Triton X-100 at RT for 10 min. Cells were blocked in 5% BSA/PBS for 1 hour at RT, followed by staining with anti-myc antibody at RT for 2 hours (Cell signaling, Cat#2278). After three washes, Alexa-488 conjugated anti-rabbit antibody (Invitrogen Cat#A11034) was added and incubated at RT for 30 min. Finally, cells were mounted in mounting media containing DAPI (Vector lab, H1200). Images were taken by DeltaVision Elite High Resolution Microscope.

Mitochondria isolation

Mitochondria were isolated from cells using a mitochondrial isolation kit (Sigma, MITOISO2) as per the manufacturer's instruction. A detailed protocol is in the supplementary.

Aconitase Enzyme Activity

ACO2 activity from the mitochondrial fraction was measured using the Aconitase Activity Assay Kit (Sigma, MAK051) according to manufacturer's protocol and normalized to the total mitochondrial protein concentration. Human prostate tumors and adjoining normal

tissues were obtained using institutionally approved IRB protocol. A detailed protocol for ACO2 activity measurement is described in the supplementary section.

Immunoprecipitation of mitochondrial ACO2 for mass-spectrometry based proteomics

C4-2 cells were transduced with ACO2-V5 adenovirus. Mitochondria were isolated and lysed with NP40 lysis buffer, followed by ACO2-V5 immunoprecipitation from mitochondrial extract. The samples were then subjected to mass spectrometry separation to detect acetylated and phosphorylated residues. A detailed protocol is provided in the supplementary section.

Immunoprecipitation

Cells were lysed using NP40 lysis buffer, supplemented with protease, and phosphatase inhibitor, and 10mM sodium butyrate (Sigma, B5887). Two mg of protein was precleared with protein A/G magnetic beads (Invitrogen, 88803) at 4°C for 1 hour. Precleared lysates were incubated with mIgG (BD, 557273), RbIgG (Millipore, sc-2027), anti-Ac-K antibody (Cell signaling, 9681) or ACO2 (Cell signaling, 6571) along with protein A/G magnetic beads at 4°C overnight. For myc-ACO2 pulldown, myc-magnetic beads (Pierce, 88843) were used. After overnight incubation, magnetic beads were washed three times with IP wash buffer (TBS containing 0.05% Tween 20 and 0.5 M NaCl). IP products were eluted by adding 100 μl 2X SDS sample buffer and boiled at 95 °C for 5 minutes. ACO2 acetylation was detected by immunoblotting.

Chromatin immuno-precipitation (ChIP) followed by qPCR

ChIP assays were performed using ChIP-IT Express Enzymatic kit (Active Motif, 53009) as described earlier (13) with some modifications. C4-2-shNT, C4-2-shSRC-2, 22Rv1-shNT and 22Rv1-shSRC-2 cells were grown in 15cm^2 plate until 80% confluency. After cross-linking protein to DNA, samples were enzymatically sheared for 30min. ChIP was performed using 5-7μg of SRC-2 (Cat#sc-8996, Santa Cruz), AR (Cat#sc-816, Santa Cruz), HDAC-2 (Cat#39533, Active Motif), Mouse IgG control (Cat#12-311, Millipore) and Rabbit-IgG control (Cat#sc-2027, Santa Cruz) antibodies. qPCR was performed with eluted ChIP DNA using specific SIRT3 promoter primers (supplementary section).

Immunohistochemistry

Tumors were fixed and stained with primary antibodies ACO2 (Cell Signaling, 6571), Ki67 (Dako, M72K0), Firefly luciferase Antibody (Thermo, MA1-16880), and SIRT3 (Cell Signaling, 2627) followed by washing and incubated with secondary antibody (Thermo). Microscopy Images were taken using Leica DMi8 inverted microscope using 63X oil immersion lens (N.A.= 1.40) and EVOS M5000 Imaging System (Invitrogen). Descriptive protocol is available in Supplementary methods.

Xenograft experiments

Animal protocol was approved by Roswell Park IACUC. Male athymic nude mice (Envigo) were castrated at 6 weeks of age. At the age of 8 weeks, mice were injected with 5x10^6 cells of C4-2-WT or C4-2-ACO2-KD or with 1x10^6 cells of 22Rv1-WT or 22Rv1-ACO2-KO

mixed in PBS:matrigel (Corning, 354248) 1:1 ratio in a volume of 100μL sub-dermally on their flanks. The tumor growth was monitored and measured by Vernier calipers. Tumor volume was calculated by $V = \dfrac{\pi * d1 * \frac{d2 + d3}{2}}{6}$, where d1, d2, and d3 are diameter measurements of the tumor. The animals injected with C4-2 cell line were sacrificed after 9 weeks of injection whereas, animals injected with 22Rv1 cells were sacrificed after 8 weeks or before tumor burden reached 2cm. The tumors were removed, and the volumes were measured. The experiments were not randomized, and the investigators were not blinded to allocation during the experiments and outcome assessment. No statistical methods were used to predetermine the sample size estimate.

Intra-iliac artery (IIA) bone metastasis

Male athymic nude mice were obtained from Envigo and IIA injections were performed as described by Wang et al (14, 15). Briefly, mice were anesthetized and restrained, and a 1.5 cm incision was made on the skin along the line between the femoral and ilium bones. The common iliac artery was exposed by removing the muscles and cancer cells suspended in 0.1 ml PBS were injected using 31G needles. C4-2-luc cells stably expressing NT-shRNA (C4-2-NT) or shRNA targeting SRC-2 (C4-2-shSRC-2) were injected (n=9, each group). The wound was sutured, and the mouse was monitored until awake and moving normally. Animals were monitored for bone metastasis progression every week by noninvasive bioluminescence measurement with IVIS Lumina II equipment. Twelve weeks after injection animals were euthanized, imaged by BLI, and bone tissues were collected and fixed. Paraffin-embedded bone samples were also subjected to hematoxylin and eosin staining to reveal the size and number of micro-metastases. The experiments were not randomized, and the investigators were not blinded to allocation during experiments and outcome assessment. No statistical methods were used to predetermine the sample size estimate.

Results

ACO2 promotes prostate tumor growth and survival

To define the functional role of ACO2 in prostate cancer, we performed gene deletion studies using an all-in-one CRISPR-Cas9 lentiviral vector system. Three different single guide RNAs (sgRNAs) targeting ACO2 were designed, and lentiviral particles were generated to transduce C4-2 cells, and stable pooled clones were selected using puromycin. CRISPR-Cas9-sgRNA-1 expressing C4-2 cells demonstrated the highest efficiency in the ablation of ACO2 expression (C4-2-ACO2-KD), although some antibiotic-resistant wildtype C4-2 cells were difficult to eliminate even after prolonged antibiotic selection (Figure. 1A). C4-2-ACO2-KD cells demonstrated significantly reduced growth on day 5, and viability on day 6 compared to C4-2-WT cells (Figure. 1B and S1A). Similarly, in 22Rv1 cells, stable depletion of ACO2 (Figure. 1C) significantly reduced the growth of ACO2-knockout (ACO2-KO) # 1 (ACO2-KO1) and #2 (ACO2-KO2) (Figure. 1D). To negate the possibility that stable ablation of ACO2 by long-term antibiotic selection may promote compensatory pathways, we performed acute-knockdown of ACO2 in C4-2 cells using short-hairpin RNA (shRNA) targeting against ACO2 (shACO2). Knockdown of ACO2 was achieved at both the

protein and mRNA levels by transducing C4-2 cells with lentivirus harboring shACO2 (Figure. S1B and S1C). Similar to stable depletion of ACO2, transient knockdown by shACO2 also showed a significant reduction in growth and viability compared to non-targeting shRNA (shNT) expressing C4-2 cells (Figure. S1D and S1E). These data indicate that ACO2 enzyme plays an important role in growth and viability of prostate cancer cells. Next, we investigated *in vivo* functions of ACO2 in prostate cancer progression. To identify an appropriate prostate cancer model for the xenograft experiment, we analyzed expression of ACO2 in prostate cancer cell lines. Analysis of ACO2 expression revealed increased levels in AR-positive lines LNCaP, C4-2, VCaP and 22Rv1 compared to AR-negative lines DU-145 and PC3, and normal prostate epithelial line RWPE-1. We selected two AR-positive lines C4-2 and 22Rv1 which are known to form tumors in immunocompromised mice (Fig. S2A, S2B and S2C). We implanted C4-2 and 22Rv1 either wildtype (WT) or knockout (KO) cells subcutaneously on the flanks of male athymic nude mice, two weeks after they were surgically castrated (Figure. 1E). Although the mean tumor volume of the C4-2 bearing animals was small, the growth of ACO2-ablated tumors was significantly slower compared to that of C4-2-WT tumors (Figure. 1F). There was one outlier mouse in the C4-2-ACO2-KD group, of which the tumor growth was rapid, and the animal had to be sacrificed within 3 weeks (marked grey-Figure. 1F). Immunohistochemical (IHC) analysis confirmed C4-2-WT tumors were positively stained for human Ki67 and human ACO2 protein; whereas ACO2-depleted tumors were negatively stained (Figure. S3A). A strong association of ACO2 and Ki67 immunostaining (nuclear) was observed in C4-2-WT tumors suggesting that ACO2 drives tumor cell proliferation. Similarly, implantation of 22Rv1 cells harboring ACO2 deletion (KO1 and KO2) resulted in reduced tumor growth compared to 22Rv1-WT in castrated male nude mice (Figure 1G and S3B). One of the animals bearing 22Rv1-WT tumor achieved the maximum allowed tumor volume by 6-weeks (marked[#]) (Figure. 1G, S3B, and S3C). *Ex vivo* analysis of the tumors indicated steady maintenance of reduced ACO2 expression in ACO2-KO tumors compared to WT, although some ACO2 expression were seen in the KO tumors which could be from the infiltrating host cells (Figure. 1H, 1I). Pathological evaluation confirmed that the ACO2-KO tumors were less proliferative than the WT tumors as indicated by Ki67 staining (Figure. 1I and 1J). Our studies confirmed that ACO2 is essential to promote prostate tumor progression and growth in castrated mice.

ACO2 promotes mitochondrial programming to facilitate citrate metabolism

Since ACO2 is a tri-carboxylic acid (TCA) cycle enzyme, we investigated whether the loss of ACO2 affects mitochondrial functions. We analyzed bioenergetic parameters of C4-2-WT and C4-2-ACO2-KD cells using a Seahorse XF analyzer and observed that genetic loss of ACO2 significantly lowered the oxygen consumption rates (OCR) suggesting reduced mitochondrial activity compared to C4-2-WT cells (Figure. 2A). Perturbation of ACO2 significantly diminished the basal metabolic rate, while oligomycin treatment decreased oxygen consumption in both C4-2-WT and C4-2-ACO2-KD cells (Figure. 2A, refer to 19-45 min time frame, S3D), however, addition of an uncoupler FCCP (Carbonyl cyanide 4-(trifluoromethoxy)phenylhydrazone) dramatically enhanced the OCR only in C4-2-WT cells (Figure. 2A, refer to 53-70 min time frame). Thus, the loss of ACO2 significantly impacted the maximal respiratory capacity of C4-2 cells (Figure. S3E). Since prostate cancer cells show increased uptake, metabolism, and dependency on glutamine (7, 16), we investigated

whether ACO2 depletion affects glutamine-dependent mitochondrial activity. C4-2 cells were transiently transduced with NTshRNA or shACO2 lentivirus and then cultured in glutamine deprived media or in the presence of 2mM glutamine followed by measurement of OCR using Seahorse XF analyzer. Glutamine deprivation reduced the OCR of NTshRNA expressing C4-2 cells to a level similar to ACO2 depleted cells growing in the presence of glutamine (Figure. 2B), indicating that the loss of ACO2 simulates a glutamine deprived condition. Although glutamine deprivation showed some effects in ACO2-depleted cells, it was not statistically significant. Since glutamine metabolism leads to lipogenesis (17), we cultured C4-2-WT and C4-2-ACO2-KD cells either in the presence or absence of glutamine followed by staining with Oil Red to analyze the total neutral lipid content. Oil Red-O staining revealed an increase in total lipid accumulation following glutamine stimulation for 3 days; however, ACO2 depletion markedly reduced lipid content in C4-2cells (Figure. 2C). Glutamine is metabolized to glutamate and then converted to α-ketoglutarate (AKG), serving as an entry point into the mitochondrial TCA cycle (17, 18). In the mitochondria, α-ketoglutarate is converted into citrate either by oxidative or reductive carboxylation. Reductive carboxylation involves the reversal of two TCA enzymes including isocitrate dehydrogenase (IDH) and ACO2. Using glutamine isotope tracers universally labeled with C^{13} ([U-^{13}C]glutamine), we confirmed that ACO2 deletion significantly reduced the incorporation of glutamine carbon into citrate. Analysis of citrate isotopomers revealed both oxidative and reductive carboxylation of glutamine-derived AKG was reduced upon ACO2 depletion (Figure. 2D). Citrate (m+4) is produced by oxidative carboxylation whereas citrate (m+5) levels are only produced by reductive glutamine metabolism (where "m" denotes the nominal mass; m+5 indicates citrate containing 5 additional mass units derived from [U-^{13}C]glutamine) (Figure. 2D). Supporting this observation, we identified reduced malate (m+3) levels in ACO2 ablated cells which are derivatives of citrate (m+5) (Figure. 2E). Next, to confirm that glutamine-dependent lipid accumulation in CRPC cells is indeed regulated by mitochondrial ACO2 enzymatic activity, we performed ACO2 enzyme assay from the purified mitochondrial fractions isolated from C4-2-WT and C4-2-ACO2-KD cells (Figure. S3F). As expected, silencing of ACO2 expression significantly repressed ACO2 enzyme activity, indicating its key role in regulating mitochondrial functions in CRPC cells (Figure. 2F). Using the WT and ACO2-depleted C4-2 and 22Rv1cells (Figure. 1C and S3G), we measured the relative levels of metabolites using mass spectrometry. Metabolic profiling confirmed significantly reduced levels of lipids such as palmitic acid and oleic acid in ACO2 depleted cells compared to WT (Figure. 2G, 2H). Among the TCA intermediates, cis-aconitate, synthesized by ACO2 during the interconversion of citrate and isocitrate, was significantly reduced in ACO2 deleted cells (Figure. 2G and 2H). Collectively, metabolic profiling confirmed that ACO2 plays a critical role in regulating mitochondrial citrate synthesis required for lipogenesis in prostate cancer.

Acetylation of ACO2 at Lys258 is critical for optimal enzyme functions

Next, we investigated the mechanisms that enhance ACO2 activity in prostate cancer cells. Previous findings indicate that mitochondrial aconitase activity is regulated by acetylation in heart tissues (19). We immuno-precipitated mitochondrial ACO2 from C4-2 cells transduced with V5-tagged ACO2 adenovirus (Adv.V5-ACO2) (Figure. 3A) and subjected them to proteomics analysis for identification of post-translational modifications. Mass

spectrometric analysis revealed that ACO2 protein is acetylated only on one lysine residue (Lys258; K258) in CRPC cells (Figure. 3B). Immunoprecipitation of total acetylated-lysine proteins (pan Ac-K antibody) followed by immunoblotting with ACO2 also confirmed that endogenous ACO2 is acetylated in prostate cancer cells (Figure. S4A). Exogenous transduction of myc-ACO2 in LNCaP, C4-2, 22Rv1, and PC-3 followed by immunoprecipitation also confirmed that ACO2 is acetylated in prostate cancer cells (Figure. S4B). To determine the functional importance of Lys258 acetylation of ACO2, we generated Lys258 to arginine (Lys258Arg; K258R) acetylation deficient mutant of ACO2. We transduced C4-2 and 22Rv1 cells with myc-tagged ACO2-WT or ACO2-K258R lentivirus (Figure. 3C and S4C) followed by immunoprecipitation, which confirmed that expression of ACO2-K258R abolishes acetylation marks on ACO2 (Figure. 3D and S4D), corroborating that the enzyme is acetylated at the Lys258 site. Next, we investigated the importance of Lys258 acetylation on cellular localization of ACO2. Ectopic expression of myc-tagged ACO2-WT or ACO2-K258R followed by immunofluorescence confocal microscopy revealed Lys258 acetylation is not essential for mitochondrial localization of the ACO2 protein (Figure. 4A). Both the ACO2-WT and ACO2-K258R mutant protein localized to the mitochondria with comparable expression levels in cells, and the stability of ACO2 protein was not affected by the K258R mutation (Figure. 4A and 4B). To study the functional significance of acetylated ACO2-Lys258 in CRPC, we re-expressed ACO2-WT or ACO2-K258R in C4-2-ACO2-KD cells in which endogenous ACO2 expression has been ablated. Re-expressed protein levels of ACO2-WT and ACO2-K258R were comparable to endogenous ACO2 expression observed in C4-2-WT cells (Figure. 4C). However, only re-expression of ACO2-WT partially rescued the CRPC growth defect observed due to ACO2 ablation, whereas ACO2-K258R failed to do so (Figure. 4D), indicating Lys258 acetylation is important for ACO2 function. We then investigated the effects of Lys258Arg mutation on ACO2 enzyme activity in the mitochondria. Mitochondrial fractions were isolated, and purity of the fractions used for ACO2 enzyme assay was confirmed by the presence of mitochondrial protein Tom20 (Figure. 4E, S4E). ACO2 enzyme activity in the mitochondria is significantly reduced in acetylation deficient ACO2-K258R compared to WT-ACO2 (Figure. 4F). These studies demonstrate that Lys258 acetylation of ACO2 is important for its optimal enzyme activity and function in prostate cancer cells.

SIRT3 is transcriptionally repressed by androgen receptor and its coregulator SRC-2 to maintain elevated levels of acetylated-ACO2

High throughput proteomics experiments have previously identified acetylated-ACO2 as a target of mitochondrial deacetylase sirtuin-3 (SIRT3) both from synthetic peptide microarray screening, and acetylated proteome analysis of SIRT3 knockout mice (20-23). Based on these reports, we hypothesized that acetylation of ACO2 may be reversibly regulated by SIRT3. To address this hypothesis, HEK293T cells were transfected with WT-SIRT3 or catalytic dead mutant SIRT3-H248Y (24), followed by immunoprecipitation with ACO2 antibody to pulldown endogenous ACO2 and immunoblotting with Ac-K. Expression of WT-SIRT3 reduced acetylated-ACO2 levels compared to cells expressing catalytic dead mutant of SIRT3, indicating SIRT3 deacetylates ACO2 (Figure. 5A). Additionally, we used a murine prostate cancer cell line TRAMP-C2, which has extremely low levels of SIRT3 compared to normal prostate epithelial cell line, RWPE-1. We restored the SIRT3 levels in

TRAMP-C2 using adenovirus Adv-SIRT3, and immunoprecipitated endogenous ACO2, followed by immunoblotting for Ac-K. Immunoprecipitated ACO2 showed significantly decreased ACO2 acetylation levels in Adv-SIRT3 re-expressing cells compared to Adv-GFP control cells (Figure. 5B), suggesting that SIRT3 negatively regulates ACO2 acetylation. Restoration of SIRT3 expression in TRAMP-C2 also showed significantly reduced mitochondrial ACO2 activity compared to control cells expressing Adv-GFP (Figure. S4F, S4G). Our findings demonstrate that ACO2 is acetylated at Lys258 in prostate cancer cells and this modification is reversibly regulated by SIRT3 (Figure. 5C). In advanced prostate tumors, SIRT3 expression is predominantly repressed (Figure. S5A) (25) and has been proposed to function as a tumor suppressor (26, 27), although the molecular details are less understood. Ectopic expression of SIRT3 (Adv. SIRT3) (Figure. 5D) significantly reduced viability of C4-2 cells compared to control (Adv. GFP) (Figure. 5E), indicating SIRT3 negatively regulates tumor cell survival. To understand the mechanisms regulating reduced SIRT3 levels, we analyzed its association with known transcriptional regulators of prostate cancer progression AR and its coregulator SRC-2 in same patient datasets. We found that SIRT3 expression is significantly low in metastatic prostate cancer (Met) compared to primary tumors (Primary) (25, 28), whereas expression of SRC-2 and AR is elevated in metastatic prostate tumors (Figure. 5F and S5B). Next, we investigated whether AR and SRC-2 functionally regulate SIRT3 gene transcription to modulate ACO2 acetylation. We analyzed the chromatin occupancy of SRC-2 on the promoter of SIRT3 using an existing *in silico* analysis of SRC-2 ChIP-seq dataset (29), and identified strong enrichment of SRC-2 on the SIRT3 promoter (Figure. S5C). We performed ChIP-qPCR to directly measure the occupancy of SRC-2 on SIRT3 promoter. We found strong enrichment of SRC-2 on SIRT3 promoter in C4-2 and 22Rv1 cells compared to isotype control (IgG) or SRC-2-depleted C4-2 cells (shSRC-2, sh19) (Figure. 6A and S5D). Since SRC-2 is a known coregulator of AR, we measured AR occupancy and found it to be enriched on the SIRT3 promoter (Figure. 6A and S5D). However, depletion of SRC-2 also significantly reduced AR chromatin occupancy, suggesting coregulator binding stabilizes the AR-complex on DNA (Figure. 6A and S5D). These findings indicate that SRC-2 functions as a co-repressor of AR on the SIRT3 promoter. Expression of SIRT3 was significantly increased upon SRC-2 knockdown compared to NTshRNA expressing cells (Figure. 6B and 6C) and knockdown of AR also increased SIRT3 expression (Figure. 6D and 6E), indicating that SRC-2 associates with AR on the SIRT3 promoter and represses transcription of SIRT3 gene. Previous studies have indicated that repressive functions of SRC-2 may be mediated by recruiting histone deacetylase 2 (HDAC2) on the promoter (30). ChIP with HDAC2 antibody revealed strong occupancy of HDAC2 on the SIRT3 promoter and upon SRC-2 silencing HDAC2 recruitment on SIRT3 promoter is significantly reduced (Figure. 6F, S5E, and S5F). These data suggest that SRC-2 dependent transcriptional repression may be mediated by recruiting HDAC2 on the target gene promoter. Next, we investigated whether acetylation of ACO2 could be reduced by SRC-2 silencing. Genetic inhibition of SRC-2 increased SIRT3 protein levels by two-fold without any significant alteration in ACO2 expression (Figure.6G). To measure the levels of acetylated ACO2 in this setting, we immunoprecipitated acetylated-lysine (Ac-K) proteins followed by immunoblotting with ACO2, and observed significantly reduced levels of acetylated-ACO2 in SRC-2 silenced (sh18 and sh9) CRPC cells compared to NT-controls (Figure. 6H). These findings suggest that increased expression of SRC-2 in

prostate cancer cells represses SIRT3 expression to retain elevated levels of enzymatically active acetylated-ACO2.

Increased SRC-2 with reduced SIRT3 expression is a common genetic hallmark enriched in prostate cancer metastatic lesions

To determine the activity of ACO2 enzyme in prostate tumors, we isolated mitochondria from human prostate adenocarcinoma (n=10) and normal adjoining tissues (n=6) (31, 32), confirmed the purity of the mitochondrial fractions (Figure. S6A), and performed ACO2 enzyme assay, which demonstrated significantly increased ACO2 activity in human prostate adenocarcinoma compared to normal adjoining tissues (Figure. 7A). Analysis of SIRT3 levels in mitochondrial fractions isolated from human prostate adenocarcinoma and normal adjoining tissues revealed that SIRT3 expression was low in tumor tissue compared to adjacent tissue in two out of three prostate tumors investigated (Figure. S6B). Next, we analyzed the mRNA expression of *SIRT3* in The Cancer Genome Atlas (TCGA) database (n=498) and investigated its relationship with *SRC-2* (gene name: *NCOA2*) (33). Our findings show that their expression inversely correlates in prostate cancer patients (r = − 0.602, Figure. 7B). Expression of AR and SRC-2 was also found to be reversely correlated with SIRT3 (r= −0.597, Figure. S6C). In addition, SRC-2 was found to be significantly elevated in prostate cancer patients who experienced biochemical recurrence following initial therapy (Figure. S6D). So, to investigate whether this axis is enriched in aggressive metastatic prostate cancer, we analyzed mRNA expression of SRC-2 and SIRT3 in metastatic lesions from human prostate cancer patients using an advanced prostate cancer genomics dataset (34). We found increased SRC-2 expression in prostate cancer metastatic lesions that spread predominantly to bones, lymph nodes, and liver (Figure. S7A, S7B). These clinical associations are compatible with our experimental findings and indicate that elevated levels of SRC-2, which transcriptionally repress SIRT3 to enhance ACO2 activity, may be a compelling factor for colonization and growth in metastatic lesions.

To directly investigate whether this molecular axis is a driver of prostate tumor adaptation in the metastatic niche, we took advantage of a spontaneous bone metastasis mouse model. We selected to study prostate cancer colonization in the bone microenvironment since almost 70% of metastatic prostate cancer patients develop bone metastasis for which therapeutic opportunities are limited (35). To test this hypothesis, we used an intra-iliac artery (IIA) injection to selectively deliver C4-2 cells with stable knockdown of SRC-2 (C4-2-shSRC-2-sh19) or NTshRNA (C4-2-NT) (Figure. 7C) into the hind limb tissues (Figure. 7D). This method allows enrichment of cancer cells in the bone and bone marrow without damaging neighboring tissues, and provides sufficient time for indolent prostate cancer cells to colonize in the bone microenvironment with minimal systemic metastasis in vital organs (14, 15). After IIA injection, each animal was imaged by bioluminescence imaging (BLI), and only successfully transplanted animals were included in the study (Figure. 7D). Animals were imaged weekly and the first positive luciferase signals were observed in C4-2-WT group after 3 weeks, indicating that initial growth of the prostate cancer cells inside the bone was slow. At 12 weeks post-injection, we observed significant luciferase signals in the hind limb region of C4-2-NT transplanted animals compared to C4-2-shSRC-2 group (Figure. 7D). At this time point, certain luciferase-positive animals started to show some visible

distress, pain and limping action, and we decided to terminate the experiment. Dissected bones from each animal was imaged by BLI, which appreciably correlated with full-body BLI signals, indicating targeted delivery of CRPC cells by this approach (Figure. 7E). Luciferase signals from animals transplanted with C4-2-shSRC-2 were significantly reduced compared to C4-2-NT group, indicating the importance of the SRC-2 axis in driving bone colonization (Figure. 7E and 7F). Histology of the bone sections confirmed the presence of C4-2 cells growing inside an osteogenic niche indicating the luciferase signals indeed originated from bone metastatic lesions (Figure. 7G). Immunohistochemical analyses of bone sections demonstrated increased expression of SIRT3 associated with micro-metastatic lesions (positively stained with luciferase antibody) originating from SRC-2 depleted C4-2 cells compared to C4-2-NT (Figure. S7C), suggesting that upregulation of SIRT3 can reduce prostate cancer bone metastasis. Collectively, our *in vivo* experimental findings substantiate the clinical association data demonstrating that the increased levels of SRC-2, which represses SIRT3 to enhance ACO2 activity, is a preeminent factor driving prostate cancer survival and growth in the bone metastatic niche (Figure. S7D).

Discussion

While oncogenesis initiates in the primary prostate, metastasis remains the leading cause of death. Notably, prostate tumors metastasize to specific organs such as liver, lymph nodes and most frequently bone. Our study revealed a distinct genetic alteration that drives metabolic adaptation of tumor cells for survival and successful homing in the bone. In particular, we demonstrated that the notable oncogene SRC-2 functions as a transcriptional repressor of the SIRT3 gene to retain elevated levels of enzymatically active acetylated-ACO2. This process favors increased tumor cell survival, growth, enhanced bioenergetic capabilities, and lipid metabolism, all of which are vital for providing sufficient metabolic flexibility to thrive in distant organs.

Mitochondrial ACO2 enzyme belongs to the family of iron-sulfur containing dehydratases, which regulates oxygen-dependent ATP biosynthesis as well as maintains citrate pool for lipogenesis. In absence of the competitive inhibitor zinc, the repressive brakes on the ACO2 enzyme were removed (36), and our study demonstrated that acetylation on lys258 functions as an activation mark that propels the enzyme activity to maintain a steady and rapid synthesis of citrate. Interestingly, we found increased levels of acetylated-ACO2 in mitochondria are perpetuated by silencing the expression of mitochondrial deacetylase SIRT3. Earlier reports have indicated that mice with genetic deletion of SIRT3 increase hyperacetylation of ACO2 in multiple tissues, suggesting acetylated-ACO2 is a direct substrate of SIRT3 (37, 38). In this study, we demonstrate a novel transcriptional regulation of SIRT3 by the AR-coregulator SRC-2(39, 40) which binds to the promoter of SIRT3 to silence gene expression. Reduced SIRT3 retains acetylated-ACO2 in the mitochondria facilitating its enhanced enzymatic activity in prostate tumors compared to adjoining normal tissues. Previous studies have shown that increased expression of SRC-2 is associated with aggressive prostate cancer however the mechanisms that accentuate the survival and growth of SRC-2 high tumors in distant organs were poorly understood (6). Our study discovered that patients with high SRC-2 concomitantly expressed low SIRT3, facilitating increased mitochondrial metabolism to sustain the survival and homing in distant metastatic sites. In a

bone metastatic mouse model, loss of SRC-2 significantly reduced metastatic growth of prostate cancer cells in the bone microenvironment, suggesting this distinct axis is required for survival and adaptation in the osteogenic niche. In summary, our study reveals the importance of mitochondrial metabolic adaptation in the development of advanced bone metastatic prostate cancer and suggests blocking SRC-2 to enhance SIRT3 expression may be therapeutically valuable.

Supplementary Material

Refer to Web version on PubMed Central for supplementary material.

Acknowledgements

References

1. Cantor JR, Sabatini DM. Cancer cell metabolism: one hallmark, many faces. Cancer discovery. 2012;2(10):881–98. [PubMed: 23009760]

2. Pascual G, Dominguez D, Benitah SA. The contributions of cancer cell metabolism to metastasis. Disease models & mechanisms. 2018;11(8):10.1242/dmm.032920.

3. Zadra G, Photopoulos C, Loda M. The fat side of prostate cancer. Biochimica et biophysica acta. 2013;1831(10):1518–32. [PubMed: 23562839]

4. Menendez JA, Lupu R. Fatty acid synthase and the lipogenic phenotype in cancer pathogenesis. Nature reviewsCancer. 2007;7(10):763–77.

5. Li X, Chen YT, Hu P, Huang WC. Fatostatin displays high antitumor activity in prostate cancer by blocking SREBP-regulated metabolic pathways and androgen receptor signaling. Molecular cancer therapeutics. 2014;13(4):855–66. [PubMed: 24493696]

6. Taylor BS, Schultz N, Hieronymus H, Gopalan A, Xiao Y, Carver BS, et al. Integrative genomic profiling of human prostate cancer. Cancer cell. 2010;18(1):11–22. [PubMed: 20579941]

7. Dasgupta S, Putluri N, Long W, Zhang B, Wang J, Kaushik AK, et al. Coactivator SRC-2-dependent metabolic reprograming mediates prostate cancer survival and metastasis. The Journal of clinical investigation. 2015;125(3):1174–88. [PubMed: 25664849]

8. Currie E, Schulze A, Zechner R, Walther TC, Farese RV Jr. Cellular Fatty Acid metabolism and cancer. Cell metabolism. 2013;18(2):153–61. [PubMed: 23791484]

9. Bertilsson H, Tessem MB, Flatberg A, Viset T, Gribbestad I, Angelsen A, et al. Changes in gene transcription underlying the aberrant citrate and choline metabolism in human prostate cancer samples. Clinical cancer research : an official journal of the American Association for Cancer Research. 2012;18(12):3261–9. [PubMed: 22510345]

10. Costello LC, Liu Y, Franklin RB, Kennedy MC. Zinc inhibition of mitochondrial aconitase and its importance in citrate metabolism of prostate epithelial cells. The Journal of biological chemistry. 1997;272(46):28875–81. [PubMed: 9360955]

11. Singh KK, Desouki MM, Franklin RB, Costello LC. Mitochondrial aconitase and citrate metabolism in malignant and nonmalignant human prostate tissues. Molecular cancer. 2006;5:14. [PubMed: 16595004]

12. Twum-Ampofo J, Fu DX, Passaniti A, Hussain A, Siddiqui MM. Metabolic targets for potential prostate cancer therapeutics. Current opinion in oncology. 2016;28(3):241–7. [PubMed: 26907571]

13. Dasgupta S, Rajapakshe K, Zhu B, Nikolai BC, Yi P, Putluri N, et al. Metabolic enzyme PFKFB4 activates transcriptional coactivator SRC-3 to drive breast cancer. Nature. 2018;556(7700):249–54. [PubMed: 29615789]

14. Wang H, Yu C, Gao X, Welte T, Muscarella AM, Tian L, et al. The osteogenic niche promotes early-stage bone colonization of disseminated breast cancer cells. Cancer cell. 2015;27(2):193–210. [PubMed: 25600338]

15. Yu C, Wang H, Muscarella A, Goldstein A, Zeng HC, Bae Y, et al. Intra-iliac Artery Injection for Efficient and Selective Modeling of Microscopic Bone Metastasis. Journal of visualized experiments : JoVE. 2016;(115). doi(115):10.3791/53982.

16. Wang Q, Hardie RA, Hoy AJ, van Geldermalsen M, Gao D, Fazli L, et al. Targeting ASCT2-mediated glutamine uptake blocks prostate cancer growth and tumour development. The Journal of pathology. 2015;236(3):278–89. [PubMed: 25693838]

17. Metallo CM, Gameiro PA, Bell EL, Mattaini KR, Yang J, Hiller K, et al. Reductive glutamine metabolism by IDH1 mediates lipogenesis under hypoxia. Nature. 2011;481(7381):380–4. [PubMed: 22101433]

18. Mullen AR, Wheaton WW, Jin ES, Chen PH, Sullivan LB, Cheng T, et al. Reductive carboxylation supports growth in tumour cells with defective mitochondria. Nature. 2011;481(7381):385–8. [PubMed: 22101431]

19. Fernandes J, Weddle A, Kinter CS, Humphries KM, Mather T, Szweda LI, et al. Lysine Acetylation Activates Mitochondrial Aconitase in the Heart. Biochemistry. 2015;54(25):4008–18. [PubMed: 26061789]

20. Still AJ, Floyd BJ, Hebert AS, Bingman CA, Carson JJ, Gunderson DR, et al. Quantification of mitochondrial acetylation dynamics highlights prominent sites of metabolic regulation. The Journal of biological chemistry. 2013;288(36):26209–19. [PubMed: 23864654]

21. Kim SC, Sprung R, Chen Y, Xu Y, Ball H, Pei J, et al. Substrate and functional diversity of lysine acetylation revealed by a proteomics survey. Molecular cell. 2006;23(4):607–18. [PubMed: 16916647]

22. Hebert AS, Dittenhafer-Reed KE, Yu W, Bailey DJ, Selen ES, Boersma MD, et al. Calorie restriction and SIRT3 trigger global reprogramming of the mitochondrial protein acetylome. Molecular cell. 2013;49(1):186–99. [PubMed: 23201123]

23. Rardin MJ, Newman JC, Held JM, Cusack MP, Sorensen DJ, Li B, et al. Label-free quantitative proteomics of the lysine acetylome in mitochondria identifies substrates of SIRT3 in metabolic pathways. Proceedings of the National Academy of Sciences of the United States of America. 2013;110(16):6601–6. [PubMed: 23576753]

24. Hirschey MD, Shimazu T, Goetzman E, Jing E, Schwer B, Lombard DB, et al. SIRT3 regulates mitochondrial fatty-acid oxidation by reversible enzyme deacetylation. Nature. 2010;464(7285):121–5. [PubMed: 20203611]

25. Grasso CS, Wu YM, Robinson DR, Cao X, Dhanasekaran SM, Khan AP, et al. The mutational landscape of lethal castration-resistant prostate cancer. Nature. 2012;487(7406):239–43. [PubMed: 22722839]

26. Quan Y, Wang N, Chen Q, Xu J, Cheng W, Di M, et al. SIRT3 inhibits prostate cancer by destabilizing oncoprotein c-MYC through regulation of the PI3K/Akt pathway. Oncotarget. 2015.

27. Li R, Quan Y, Xia W. SIRT3 inhibits prostate cancer metastasis through regulation of FOXO3A by suppressing Wnt/beta-catenin pathway. Experimental cell research. 2018;364(2):143–51. [PubMed: 29421536]

28. Tomlins SA, Mehra R, Rhodes DR, Cao X, Wang L, Dhanasekaran SM, et al. Integrative molecular concept modeling of prostate cancer progression. Nat Genet. 2007;39(1):41–51. [PubMed: 17173048]

29. Zhu B, Gates LA, Stashi E, Dasgupta S, Gonzales N, Dean A, et al. Coactivator-Dependent Oscillation of Chromatin Accessibility Dictates Circadian Gene Amplitude via REV-ERB Loading. Molecular cell. 2015;60(5):769–83. [PubMed: 26611104]

30. Uhlenhaut NH, Barish GD, Yu RT, Downes M, Karunasiri M, Liddle C, et al. Insights into negative regulation by the glucocorticoid receptor from genome-wide profiling of inflammatory cistromes. Molecular cell. 2013;49(1):158–71. [PubMed: 23159735]

31. Fanshier DW, Gottwald LK, Kun E. Enzymatic Synthesis of Monofluorocitrate from β-Fluoro-oxaloacetate. Journal of Biological Chemistry. 1962;237(12):3588–96.

32. Fillebeen C, Caltagirone A, Martelli A, Moulis JM, Pantopoulos K. IRP1 Ser-711 is a phosphorylation site, critical for regulation of RNA-binding and aconitase activities. The Biochemical journal. 2005;388(Pt 1):143–50. [PubMed: 15636585]

33. Cancer Genome Atlas Research N. The Molecular Taxonomy of Primary Prostate Cancer. Cell. 2015;163(4):1011–25. [PubMed: 26544944]

34. Robinson D, Van Allen EM, Wu YM, Schultz N, Lonigro RJ, Mosquera JM, et al. Integrative clinical genomics of advanced prostate cancer. Cell. 2015;161(5):1215–28. [PubMed: 26000489]

35. Dasgupta S, Srinidhi S, Vishwanatha JK. Oncogenic activation in prostate cancer progression and metastasis: Molecular insights and future challenges. Journal of carcinogenesis. 2012;11:4. [PubMed: 22438770]

36. Costello LC, Feng P, Milon B, Tan M, Franklin RB. Role of zinc in the pathogenesis and treatment of prostate cancer: critical issues to resolve. Prostate cancer and prostatic diseases. 2004;7(2):111–7. [PubMed: 15175662]

37. Peterson BS, Campbell JE, Ilkayeva O, Grimsrud PA, Hirschey MD, Newgard CB. Remodeling of the Acetylproteome by SIRT3 Manipulation Fails to Affect Insulin Secretion or beta Cell Metabolism in the Absence of Overnutrition. Cell Rep. 2018;24(1):209–23.e6. [PubMed: 29972782]

38. Dittenhafer-Reed KE, Richards AL, Fan J, Smallegan MJ, Fotuhi Siahpirani A, Kemmerer ZA, et al. SIRT3 mediates multi-tissue coupling for metabolic fuel switching. Cell Metab. 2015;21(4):637–46. [PubMed: 25863253]

39. Dasgupta S, Lonard DM, O'Malley BW. Nuclear receptor coactivators: master regulators of human health and disease. Annual Review of Medicine. 2014;65:279–92.

40. Dasgupta S, O'Malley BW. Transcriptional coregulators: emerging roles of SRC family of coactivators in disease pathology. Journal of Molecular Endocrinology. 2014;53(2):R47–59. [PubMed: 25024406]
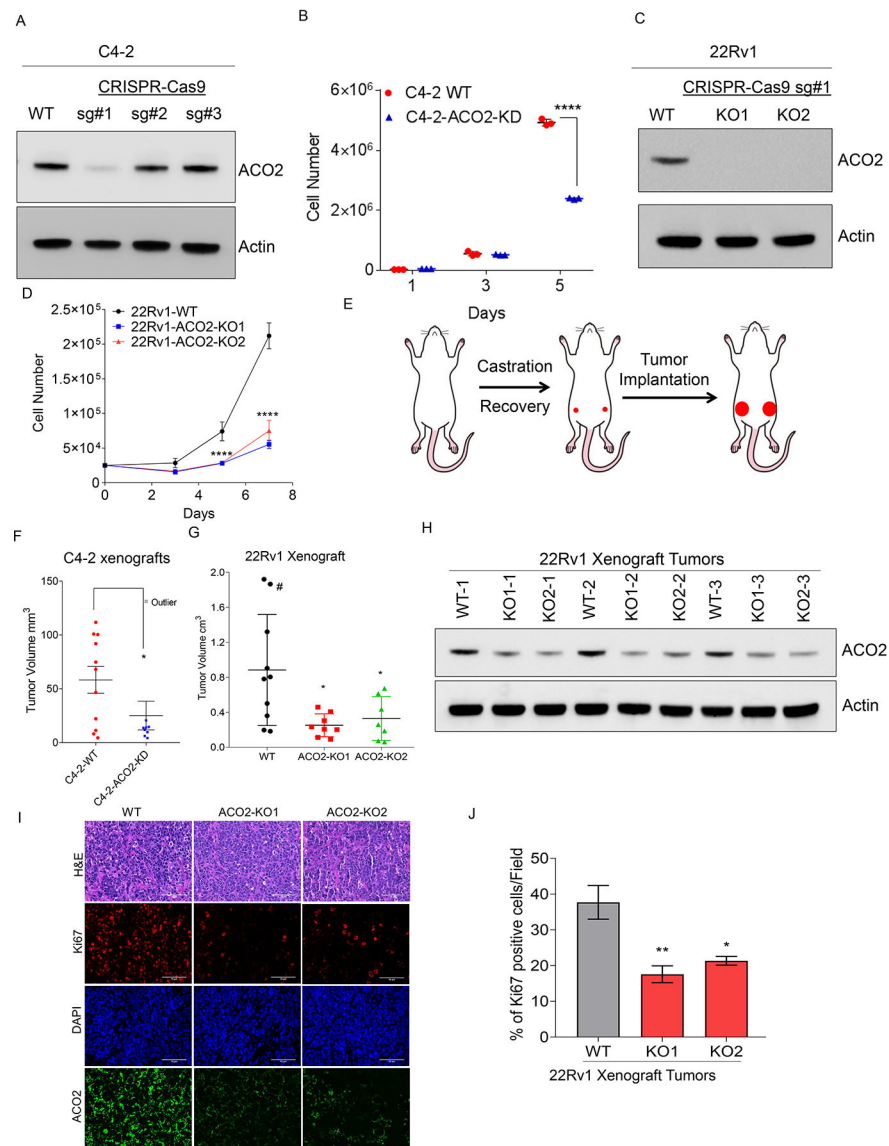
Significance

This study highlights the importance of mitochondrial aconitase activity in the development of advanced metastatic prostate cancer and suggests that blocking SRC-2 to enhance SIRT3 expression may be therapeutically valuable.

Figure 1. Mitochondrial aconitase (ACO2) drives prostate tumorigenesis.

(A) CRISPR-Cas9 mediated stable targeting of ACO2 gene in C4-2 cells using three independent sgRNAs were confirmed by immunoblotting Wild Type (WT) and Knockdown (ACO2-KD) pooled clones. Actin was used as a loading control.

(B) C4-2-WT and C4-2-ACO2-KD cells (n=3, each group) were counted on days 1, 3, and 5. Data are shown in mean ± S.D. ****P<0.000001, two-way ANOVA with Tukey's multi comparison test.

(C) CRISPR-Cas9 mediated stable targeting of ACO2 gene in 22Rv1 cells using sgRNA#1 was confirmed by immunoblotting using Wild Type (WT) and two pooled Knockout (KO1 and KO2). Actin was used as a loading control.

(D) 22Rv1-WT, 22Rv1-ACO2-KO1, and 22Rv1-ACO2-KO2 cells (n=3, each group) were counted on days 3, 5, and 7. Data are shown in mean ± S.D. ****P<0.0001, two-way ANOVA with Tukey's multi comparison test.

(E) Schematics of the *in vivo* xenograft experiment. Male athymic nude mice were surgically castrated followed by implantation of prostate cancer cells C4-2 or 22Rv1 WT or ACO2-depleted lines. After 9 weeks primary tumors were resected out.

(F) C4-2-ACO2-WT (n=11) and C4-2-ACO2-KD (n=9) were injected subcutaneously and tumor volume after 9 weeks are shown. Data are shown in mean ± S.E.M. *P=0.0466, Kolmogorov-Smirnov test.

(G) 22Rv1-WT (n=10), 22Rv1-ACO2-KO1 (n=8), and 22Rv1-ACO2-KO2 (n=7) were injected subcutaneously and xenograft tumor volumes are shown. Data are shown in mean ± S.D. WT vs KO1, *P=0.0106 and WT vs KO2, *P=0.0307 by one-way ANOVA with Dunnett's multiple comparisons test. # indicates mouse sacrificed during the 6th week.

(H) ACO2 protein levels in xenograft tumors from 22Rv1-WT (n=3), 22Rv1-ACO2-KO1 (n=3), and 22Rv1-ACO2-KO2 (n=3, individual animal from each group) with actin as a loading control.

(I) H&E staining of the 22Rv1-WT, 22Rv1-ACO2-KO1 and 22Rv1-ACO2-KO2 xenograft tumors, and immunohistochemistry for ACO2 (green), Ki67 (red), DAPI (blue) (scale bar 75 μm).

(J) Bar graphs indicating the percentage of Ki67-positive cells in the tumors. n=3 animals per group, three fields counted from each slide. Data represents mean ± S.D. *P=0.017 and **P=0.0069 by one-way ANOVA with Dunnett's multiple comparisons test.
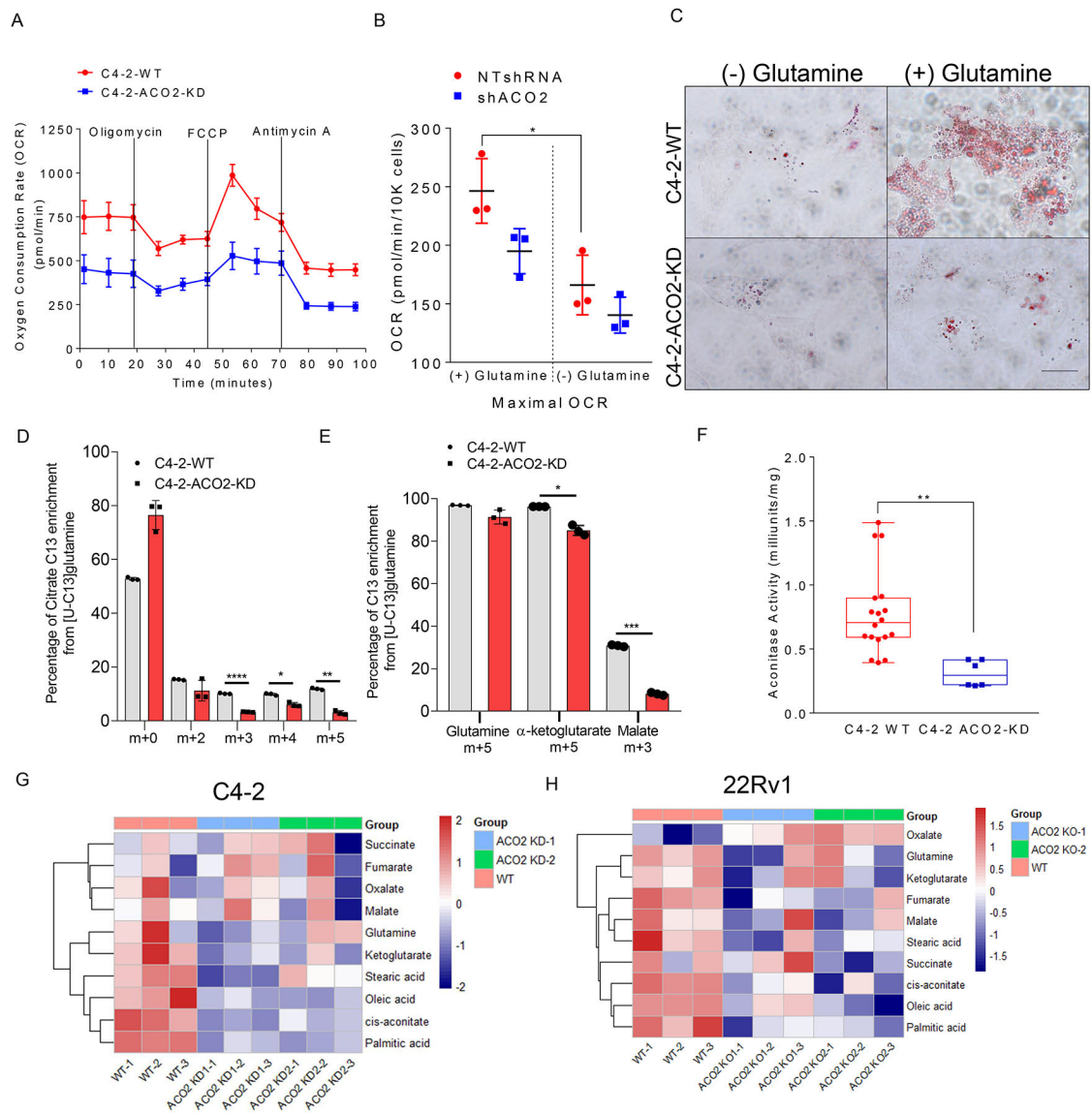
Figure 2. ACO2 regulates mitochondrial programming to promote citrate synthesis.
(A) C4-2-WT and C4-2-ACO2-KD cells (n=5, each group) were used to measure oxygen consumption rates (OCR) sequentially before and after the addition of oligomycin (2 μM), FCCP (1 μM), and antimycin A (1 μM) by XF24 Extracellular Flux Analyzer. Data are shown in mean ± S.D. Each time point is statistically significant. **** P<0.000001, two-way ANOVA with Sidak's multiple comparisons test.

(B) Acute ACO2 knockdown was induced by lentivirus pGIPZ-shNT or pGIPZ-shACO2 for 4 days in C4-2 cells (n=3, each group) and cultured overnight in regular RPMI media with or without 2mM glutamine. Maximal OCR rates were measured. Data are shown as mean ± S.D. * P=0.007012, two-way ANOVA with Sidak's multiple comparisons test.

(C) C4-2-WT and C4-2-ACO2-KD cells were stained with Oil O Red followed by microcopy (100x oil immersion). Scale bars, 40 μm.

(D) Percentage distribution of citrate C13 isotopologues in C4-2-WT and C4-2-ACO2-KD cells from L-[U-C13] glutamine after 24 hours of labeling (n=3, biological cell sample). Data are shown as mean ± S.D. *P < 0.05, **P < 0.001 and ****P < 0.0001 by 2-way ANOVA with Tukey's multiple comparisons test.

(E) Glutamine (m+5), α-ketoglutarate (m+5), and malate (m+3) labeling from L-[U-C13]glutamine in C4-2-WT and C4-2-ACO2-KD cells are shown (n=3, biological cell sample). *P < 0.05 and ***P < 0.001 by 2-way ANOVA with Tukey's multiple comparisons test.

(F) Mitochondrial fraction from C4-2-WT (n=18) and C4-2-ACO2-KD (n=6, biological sample) cells were used for ACO2 activity. Boxes represent the twenty-fifth and seventy-fifth percentiles, lines represent median, whiskers showing minimum and maximum points, and plus symbol indicates the mean. ** P=0.0028, unpaired t-test two-tailed.

(G-H) Heatmap showing the relative abundance of key TCA-cycle metabolites and selected lipids (Stearic acid, oleic acid, and palmitic acid) in (G) C4-2-WT, C4-2-ACO2-KD1 and C4-2-ACO2-KD2 cells, and (H) 22Rv1-WT, 22Rv1-ACO2-KO1 and 22Rv1-ACO2-KO2 cells. Metabolite abundance was normalized and calculated as log2 fold change compared to WT cells. Rows represent metabolites that are clustered based on euclidean distance. Columns represent WT and two different ACO2-depleted groups with n=3, biological cell samples. Statistical testing between different groups was performed using Dunnett's multiple comparisons test.
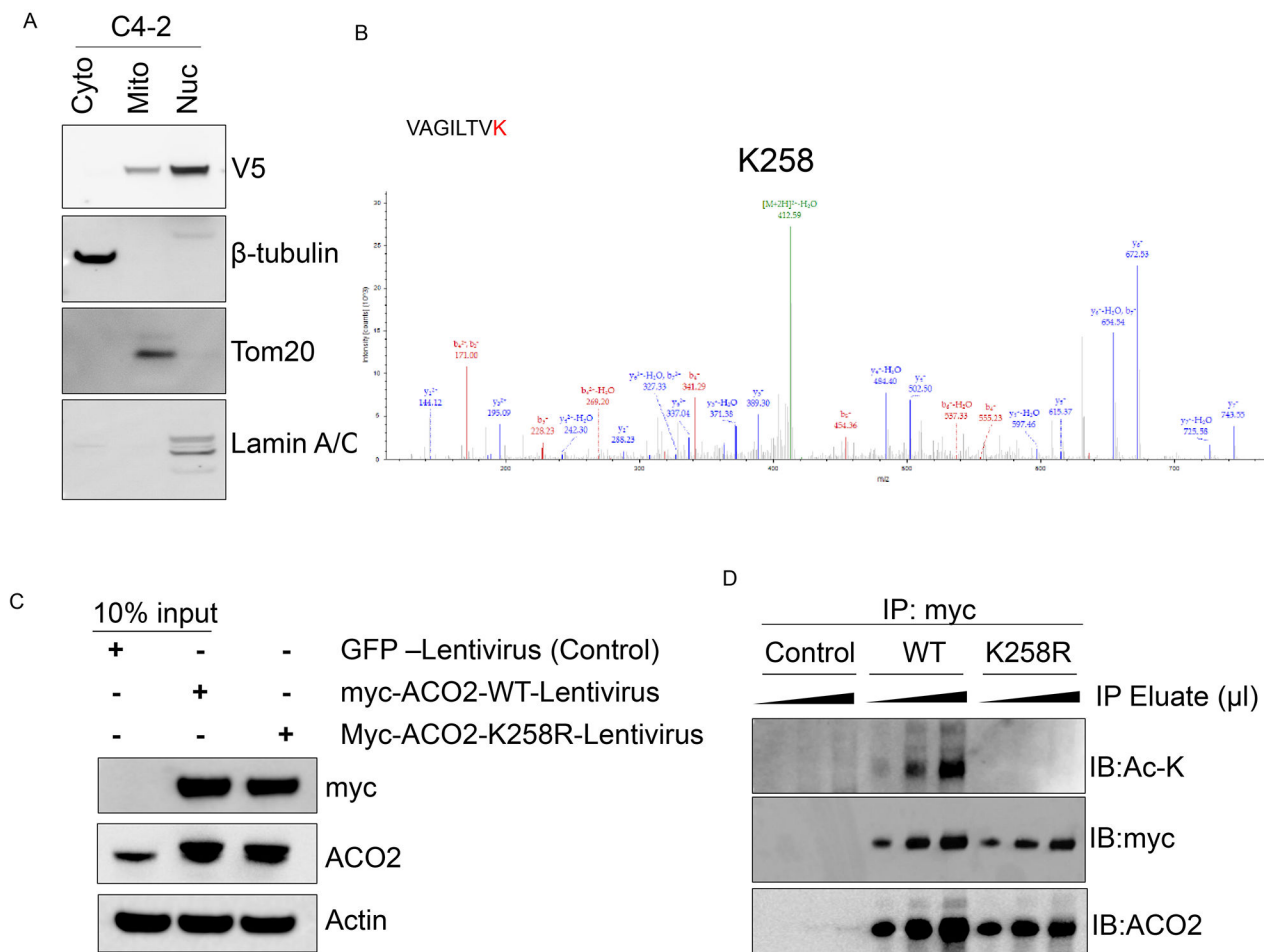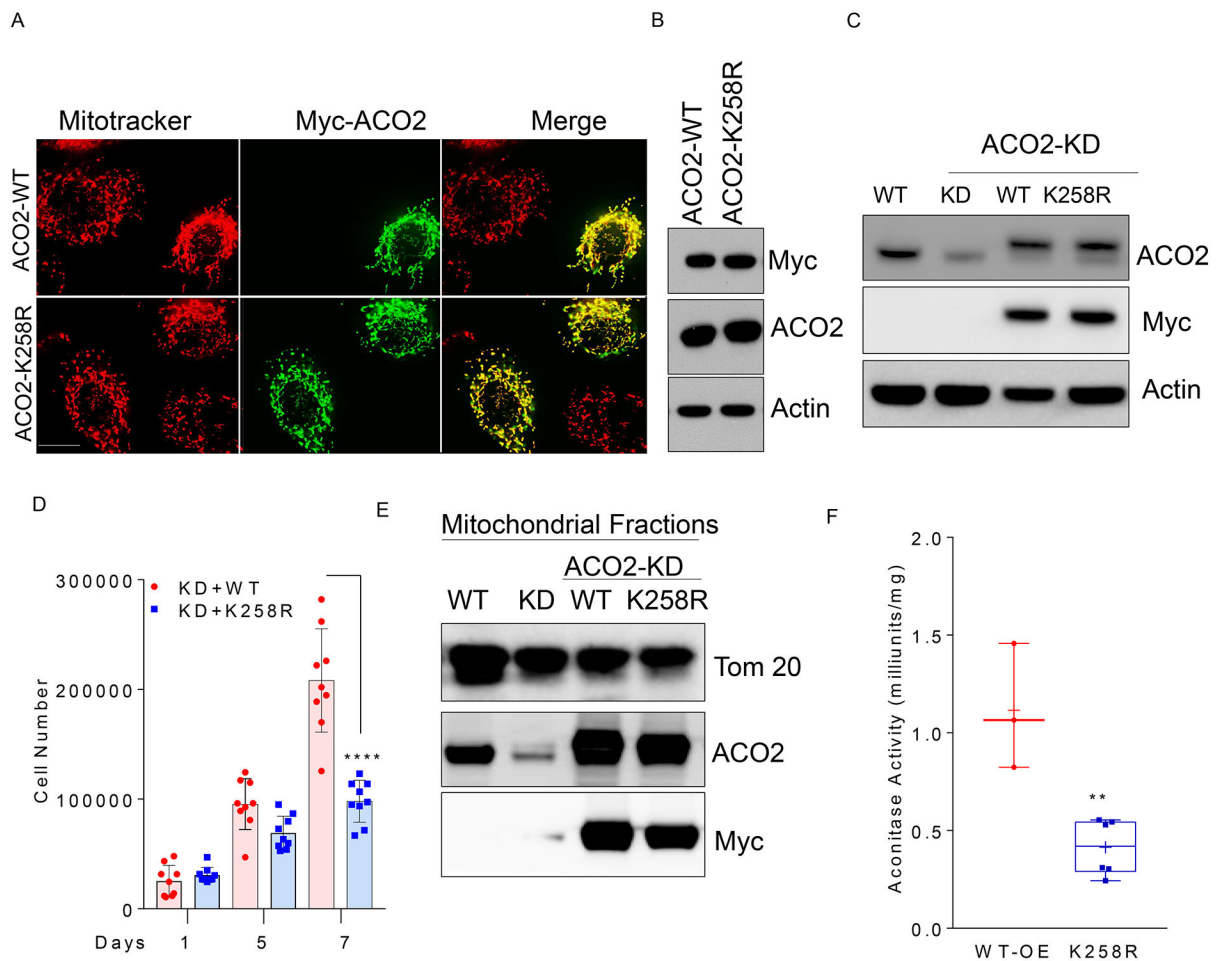
Figure 3. ACO2 enzyme is acetylated at Lys 258 residue.

(A) V5-tagged-ACO2 adenovirus were transduced to C4-2 cells fractionated into cytosolic (Cyto), mitochondrial (Mito), and nuclear (Nuc) compartments followed by immunoblotting with cytosolic, mitochondrial, and nuclear proteins β-tubulin, Tom20 and lamin A/C respectively.

(B) Mitochondrial fractions from V5-tagged ACO2 expressing C4-2 cells were (as shown in panel A) immuno-precipitated with anti-V5 antibody followed by mass spectrometric analyses. Mass spectrum shows the green acetylation peak. n = 3 biologically independent samples.

(C) C4-2-WT cells were transduced with lentivirus expressing GFP (Control), myc-ACO2-WT and myc-ACO2-K258R followed by immunoblotting with Myc, ACO2, and β-actin antibodies.

(D) Cell lysates from (C) were used for immunoprecipitation with myc-beads followed by immunoblotting with Ac-K, myc, and ACO2 antibodies. n = 3 biological cell samples.

Figure 4. Lys 258 acetylation is required for optimal ACO2 enzyme activity.

(A) PC3 cells were transfected with myc-ACO2-WT or myc-ACO2-K258R for 48 hours (n=4, each group). Immunofluorescence staining was performed with anti-myc (green) while being counterstained with mitotracker (red) and DAPI (blue) followed by confocal microscopy. Scale bars, 10 μm.

(B) Ectopic protein expression of ACO2-WT and ACO2-K258R were analyzed by immunoblotting with ACO2 and myc antibodies, and β-actin as a housekeeping loading control.

(C) Lentivirus expressing myc-ACO2-WT or myc-ACO2-K258R was transduced into C4-2-ACO2-KD cells. Re-expression was confirmed by immunoblotting with ACO2 and myc antibodies using β-actin as a housekeeping loading control.

(D) C4-2-ACO2-KD cells were transduced with myc-ACO2-WT or myc-ACO2-K258R for 4 days (n=9, each group) and counted on days 1, 5, and 7. Data are shown in mean ± S.D. **** P=0.0001, two-way ANOVA with Dunnett's multiple comparisons test.

(E) Mitochondrial fractions from WT, KD, and KD cells re-expressing myc-WT-ACO2 or myc-ACO2-K258R were immunoblotted with Tom20, ACO2 and myc antibodies.

(F) Mitochondrial fractions of C4-2 cells expressing either WT (n=3) or K258R (n=6) were used to measure ACO2 enzyme activity. The activity was normalized to the protein concentration. Boxes are as in Figure. 2D. **P=0.0021, unpaired t-test two-tailed.

Figure 5. SIRT3 functions as an ACO2-deacetylase.

(A) HEK293T cells were transduced with WT-SIRT3-Flag or HA-SIRT3-H248Y plasmid and immunoblotted for ACO2, HA, Flag, Actin, and Ac-K in input depicting WT-SIRT3-Flag or HA-SIRT3-H248Y expression. Transfected cell lysates were used for endogenous ACO2 and IgG (control) immunoprecipitation, followed by immunoblotting for ACO2 and Ac-K.

(B) Adv-GFP (control) and Adv-SIRT3 were re-expressed in TRAMP-C2 cells followed by immunoblotting for ACO2, SIRT3, Ac-K, and Actin for inputs. RWPE-1 (normal prostate cell line) was used to titer the SIRT3 re-expression level in TRAMP-C2 cells. Endogenous ACO2 or IgG (control) was immunoprecipitated, followed by immunoblotting for ACO2 and Ac-K.

(C) Schematic representation showing SIRT3 regulating acetylation-status of ACO2.

(D) C4-2 cells were transduced with Adv-GFP or Adv-SIRT3 for 8 days followed by immunoblotting with SIRT3 and β-actin antibodies. Actin was used as a loading control.

(E) C4-2 cells transduced with Adv-GFP or Adv-SIRT3 for 3 days, were used for viability assay (n=12, each group). Reading was taken at the end of 5 days. Data are shown in mean ± S.D. **** P<0.000001, unpaired t-test two-tailed.

(F) mRNA expression of SIRT3, SRC-2 (gene name: NCOA2), and AR from GSE35988 dataset using GPL9128 platform consisting of Normal n=28, Primary tumor n=59, and Met n=32. Expression of SIRT3, SRC-2, and AR in Primary vs Met, *P*<0.001.
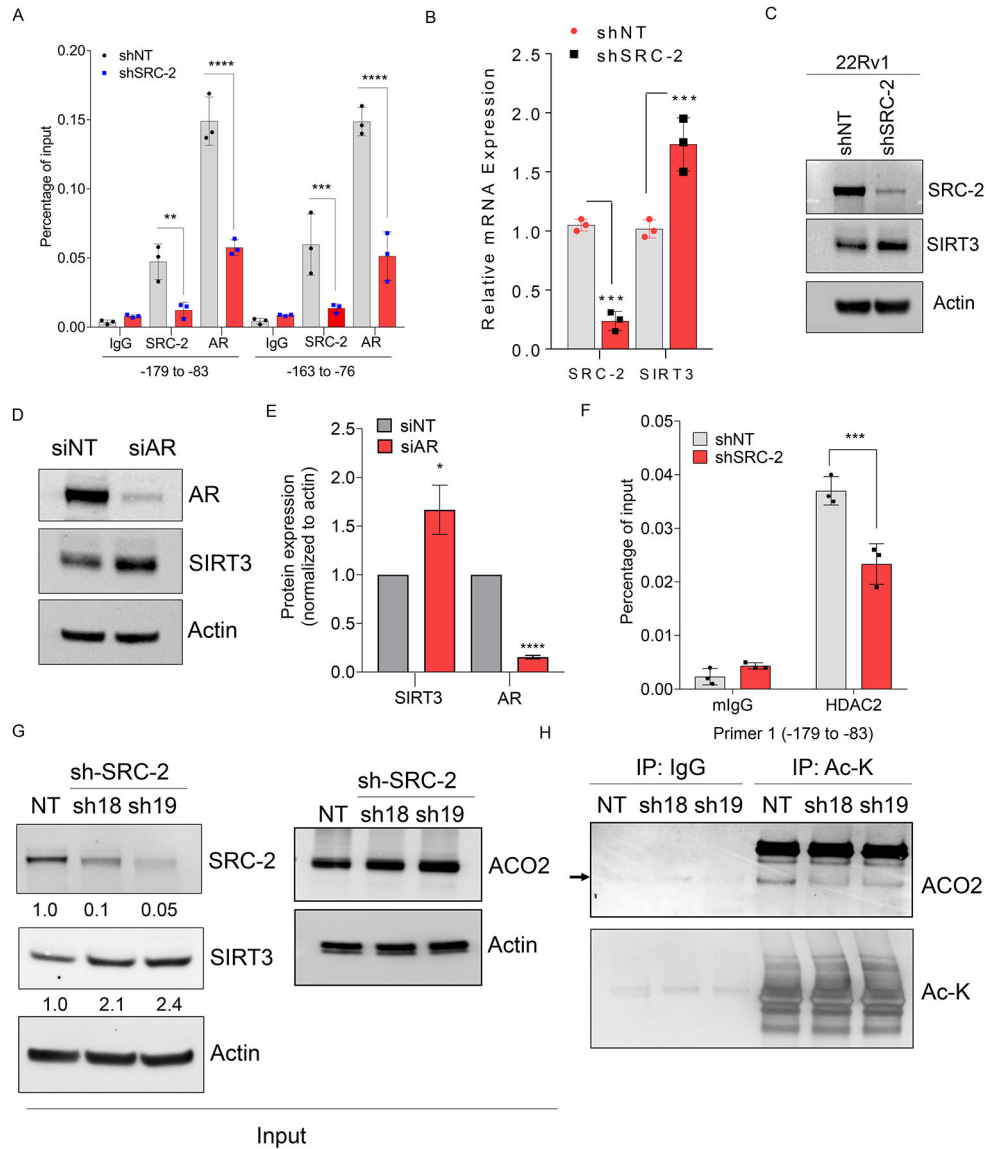
Figure 6. SIRT3 expression is repressed by transcriptional coregulator SRC-2 to retain elevated levels of acetylated-ACO2.

(A) C4-2 cells stably expressing shNT or shSRC-2 were used for chromatin immunoprecipitation (ChIP) to pull down SRC-2 and AR, followed by qPCR to measure their occupancy on SIRT3 promoter, n=3 biological sample/group. Data are shown in mean ± S.D. ** $P<0.01$, *** $P<0.001$, **** $P<0.0001$ two-way ANOVA with Sidak's multiple comparisons test.

(B) C4-2 cells stably expressing shNT or shSRC-2 were used to measure mRNA expression of SRC-2 and SIRT3, n=3 biological sample/group. Data are shown in mean ± S.D. *** $P<0.001$, two-way ANOVA with Sidak's multiple comparisons test.

(C) 22Rv1 cells stably expressing shNT or shSRC-2 (sh19) were used to measure expression of SRC-2 and SIRT3 by immunoblotting, n=3 biological cell sample. Actin was used as a loading control.

(D) C4-2 cells were transfected with siRNA targeting AR or non-targeting followed by immunoblot to measure AR and SIRT3 protein levels, n=3 biological samples/group.

(E) Densitometric analysis of immunoblots shown in (D) normalized to actin was plotted with siNT set at 1, n=3. Bar graph represents mean ± S.D. *P=0.01 and ****P<0.0001 by unpaired, two-tailed t-test.

(F) C4-2 cells stably expressing shNT or shSRC-2 were used for ChIP to pull down HDAC2, followed by qPCR to measure their occupancy on SIRT3 promoter, n=3 biological sample/ group. Data are shown in mean ± S.D. *** P<0.001, two-way ANOVA with Sidak's multiple comparisons test.

(G) Immunoblot analysis showing protein levels of SRC-2, SIRT3, and ACO2 in C4-2 cells stably expressing NT-shRNA or shRNA-SRC-2 (sh18 and sh19). Actin was used as a loading control.

(H) Inputs from C4-2 cells stably expressing NT-shRNA or shRNA-SRC-2 as shown in (G) were immunoprecipitated (IP) with isotype control (IgG) or pan-acetyl-lysine (Ac-K) antibodies followed by immunoblotting with ACO2 and Ac-K antibodies, n=3 biological replicates.
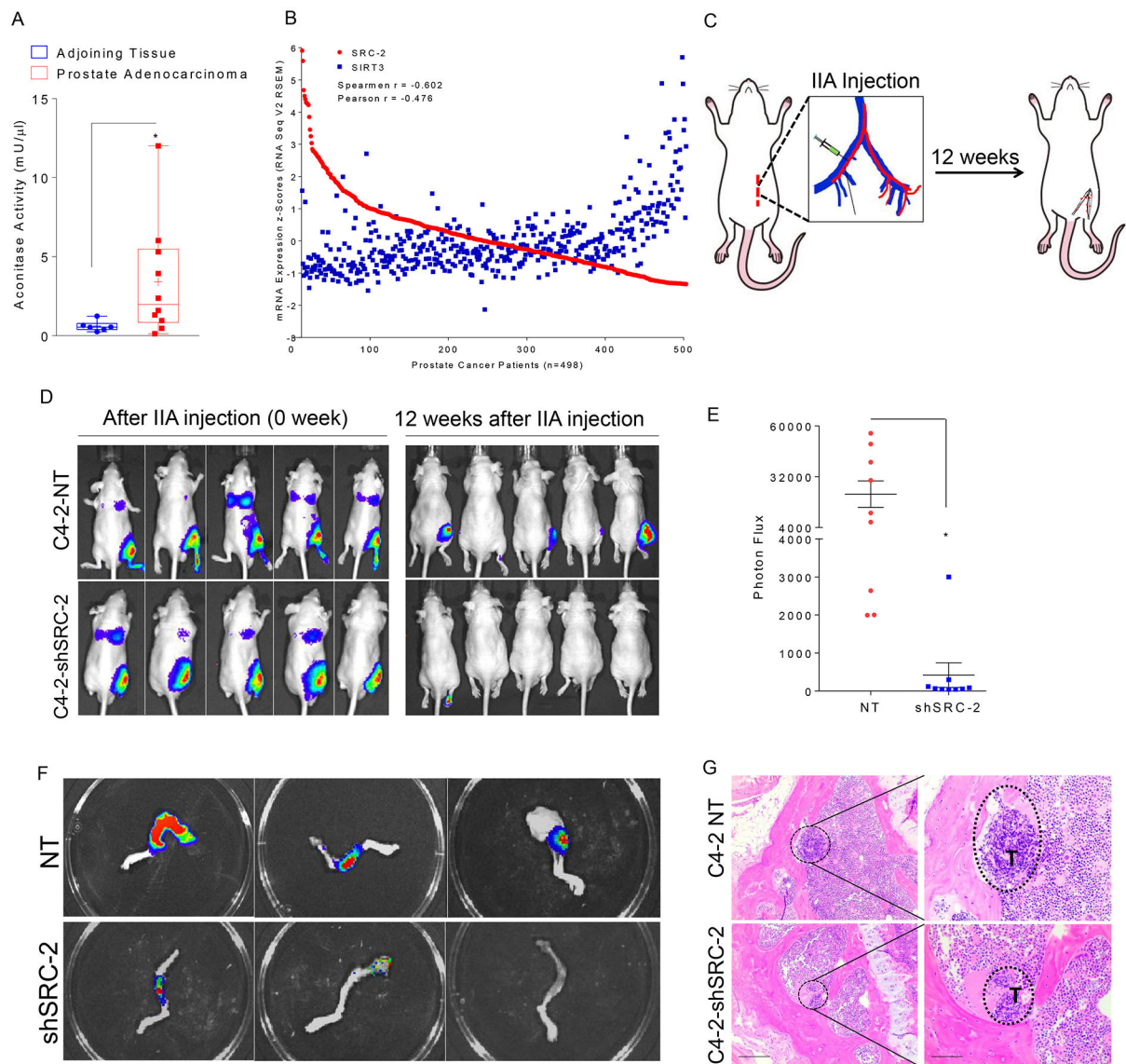
Figure 7. SIRT3 repression by SRC-2 drives aggressive metastatic prostate cancer to the bone.

(A) Aconitase enzyme activity was measured from mitochondria isolated from human prostate adenocarcinoma (n=10) and normal adjoining tissues (n=6). *P=0.0315 using Kolmogorov-Smirnov test.

(B) mRNA expression of SRC-2 and SIRT3 from TCGA database shows an inverse correlation in prostate cancer patients (n=498). Spearman r= −0.602 and Pearson r= −0.476.

(C) Schematics of the *in vivo* xenograft experiment to determine CRPC cell growth and survival in the bone. C4-2 cells stably expressing NT-shRNA (C4-2-NT) or C4-2-shSRC-2 were injected in male athymic nude mice (n=9, each group) via the intra-iliac artery (IIA) followed by bioluminescence imaging. Animals were imaged weekly for 10 weeks to monitor tumor growth in the bone.

(D) Bioluminescence imaging of mice right after IIA injection (each mouse was imaged separately) and at the end of the study, 12 weeks after IIA injection.

(E) Quantification of *ex vivo* bioluminescence signals emitted from extracted hind limb bones. Data are shown in mean ± SEM. *P=0.0003, Mann-Whitney test two-tailed.

(F) Representative images of bioluminescence signals emitted from extracted hind limb bones.

(G) H&E staining showing the histopathology of bone sections from NT and shSRC-2 groups. Scale bars, 200 μm (left) and 100 μm (right).